Scanning Probe Microscopy Studies of Carbon Nanotubes

Teri Wang Odom[1], Jason H. Hafner[1], and Charles M. Lieber[1,2]

[1] Department of Chemistry and Chemical Biology, Harvard University, Cambridge MA 02138, USA
[2] Division of Engineering and Applied Sciences, Harvard University, Cambridge MA 02138, USA

Abstract. This chapter summarizes scanning probe microscopy investigations of the properties and manipulation of carbon nanotubes, and moreover, the fabrication and utilization of nanotubes as novel tips for probe microscopy experiments. First, scanning tunneling microscopy and spectroscopy measurements that elucidate (1) the basic relationship between single-walled carbon nanotube (SWNT) atomic structure and electronic properties, (2) the one-dimensional band structure of nanotubes, (3) localized structures in SWNTs, and (4) the electronic behavior of finite size SWNTs are discussed. Second, atomic force microscopy investigations of the manipulation of nanotubes on surfaces to obtain information about nanotube-surface interactions and nanotube mechanical properties, and to create nanotube device structures are reviewed. Lastly, the fabrication, properties and application of carbon nanotube probe microscopy tips to ultrahigh resolution and chemically sensitive imaging are summarized. Prospects for future research are discussed.

Carbon nanotubes are currently the focus of intense interest worldwide. This attention to carbon nanotubes is not surprising in light of their promise to exhibit unique physical properties that could impact broad areas of science and technology, ranging from super strong composites to nanoelectronics [1–3]. Recent experimental studies have shown that carbon nanotubes are the stiffest known material [4,5] and buckle elastically (vs. fracture) under large bending or compressive strains [5,6]. These mechanical characteristics suggest that nanotubes have significant potential for advanced composites, and could be unique force transducers to the molecular world. Moreover, the remarkable electronic properties of carbon nanotubes offer great intellectual challenges and the potential for novel applications. For example, theoretical calculations first predicted that single-walled carbon nanotubes (SWNTs) could exhibit either metallic or semiconducting behavior depending only on diameter and helicity [7–9]. This ability to display fundamentally distinct electronic properties without changing the local bonding, which was recently experimentally demonstrated through atomically resolved scanning tunneling microscopy (STM) measurements [10,11] sets nanotubes apart from all other nanowire materials [12,13].

Scanning probe microscopies, such as STM and atomic force microscopy (AFM), have been exploited to interrogate the electrical and mechanical

properties of individual 1D nanostructures such as carbon nanotubes, and moreover, nanotubes have been incorporated as tips in scanning probe microscopies to enable these techniques to image with unprecedented sensitivity. In this Chapter, we will review scanning probe microscopy investigations of the fundamental properties and manipulation of carbon nanotubes, and the fabrication and use of nanotubes as novel probe tips. The basic structure of the review is as follows. First, we discuss scanning tunneling microscopy and spectroscopy measurements addressing (1) the basic relationship between SWNT atomic structure and electronic properties, (2) the one-dimensional band structure of nanotubes, (3) localized structures in SWNTs, and (4) the electronic behavior of finite size SWNTs. Second, we review AFM investigations of the manipulation of nanotubes on surfaces to obtain information about nanotube-surface interactions and nanotube mechanical properties, and to create nanotube device structures. Lastly, we discuss the fabrication and properties of carbon nanotube probe microscopy tips and the application of this new generation of probes to ultrahigh resolution and chemically sensitive imaging. Prospects for future research are discussed.

1 Expectations from Theory

SWNTs can be viewed as an extension in one-dimension (1D) of different fullerene molecular clusters or as a strip cut from an infinite graphene sheet and rolled up to form a tube (Fig. 1a). Major characteristics of their electronic properties can be built up from relatively simply Hückel-type models using p(π) atomic orbitals. The diameter and helicity of a SWNT are uniquely characterized by the roll-up vector $\boldsymbol{C}_h = \mathrm{n}\boldsymbol{a}_1 + \mathrm{m}\boldsymbol{a}_2 = (\mathrm{n,m})$ that connects crystallographically equivalent sites on a two-dimensional (2D) graphene sheet, where $\boldsymbol{a}_1$ and $\boldsymbol{a}_2$ are the graphene lattice vectors and n and m are integers. The limiting, achiral cases, (n,0) zigzag and (n,n) armchair are indicated with dashed lines in Fig. 1b.

Electronic band structure calculations predict that the (n,m) indices determine whether a SWNT will be a metal or a semiconductor [7–9]. To understand this unique ability to exhibit distinct electronic properties within an all-carbon sp^2 hybridized network, it is instructive to consider the 2D energy dispersion of graphite. Graphite is a semi-metal or zero-gap semiconductor whose valence and conduction bands touch and are degenerate at six $\mathbf{K}$ (k_F) points; these six positions define the corners of the first Brilluion zone. As a finite piece of the 2D graphene sheet is rolled up to form a 1D tube, the periodic boundary conditions imposed by $\boldsymbol{C}_h$ can be used to enumerate the allowed 1D subbands-the quantized states resulting from radial confinement-as follows:

$$\boldsymbol{C}_h \bullet \boldsymbol{k} = 2\pi q \tag{1}$$

where q is an integer. If one of these allowed subbands passes through one of the $\mathbf{K}$ points, the nanotube will be metallic, and otherwise semiconducting.

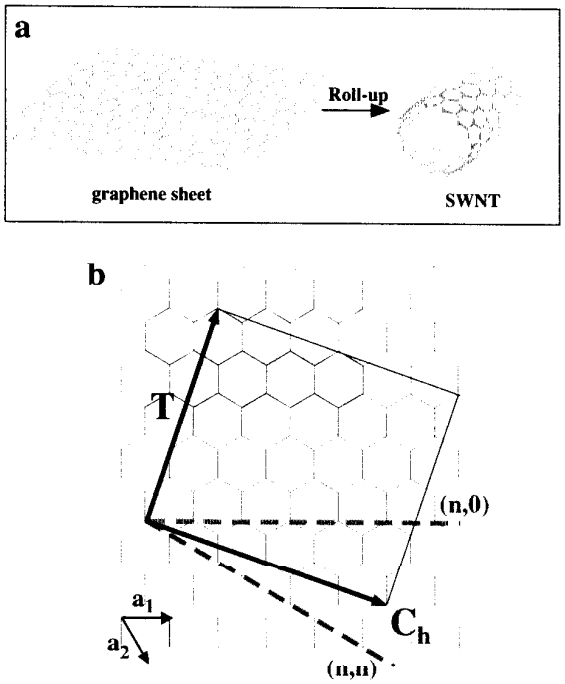

Fig. 1. Schematic diagrams of a SWNT and roll-up vector. (**a**) Graphene strip rolled into a seamless tube. (**b**) 2D graphene sheet illustrating lattice vectors $\boldsymbol{a}_1$ and $\boldsymbol{a}_2$, and the roll-up vector $\boldsymbol{C}_h = \mathrm{n}\boldsymbol{a}_1 + \mathrm{m}\boldsymbol{a}_2$. The limiting, achiral cases of (n,0) zigzag and (n,n) armchair are indicated with dashed lines. The translation vector $\boldsymbol{T}$ is along the nanotube axis and defines the 1D unit cell. The shaded, boxed area represents the unrolled unit cell formed by $\boldsymbol{T}$ and $\boldsymbol{C}_h$. The diagram is constructed for (n,m) = (4,2)

Thus to first order, zigzag (n,0) or chiral (n,m) SWNTs are metallic when (n-m)/3 is an integer and otherwise semiconducting.

Independent of helicity, the energy gaps of the semiconducting (n,0) and (n,m) tubes should depend inversely on diameter. In addition, the finite curvature of the tubes also leads to mixing of the π/σ bonding and π^*/σ^* antibonding orbitals in carbon. This mixing should cause the graphene band crossing (k_F) to shift away from the **K** point and should produce small gaps in (n,0) and (n,m) metallic tubes with the magnitude of the gap depending inversely with the square of the diameter [7,14]. However, (n,n) armchair tubes are expected to be truly metallic since k_F remains on the subband of the nanotube [15].

Away from the **K** point, signature features in the density of states (DOS) of a material appear at the band edges, and are commonly referred to as

van Hove singularities (VHS). These singularities are characteristic of the dimension of a system. In three dimensions, VHS are kinks due to the increased degeneracy of the available phase space, while in two dimensions the VHS appear as stepwise discontinuities with increasing energy. Unique to one-dimensional systems, the VHS are manifest as peaks. Hence, SWNTs and other 1D materials are expected to exhibit spikes in the DOS due to the 1D nature of their band structure.

2 Scanning Tunneling Microscopy Studies of Electronic Properties of Nanotubes

Scanning tunneling microscopy and spectroscopy (STS) offer the potential to probe these predictions about the electronic properties of carbon nanotubes since these techniques are capable of resolving simultaneously the atomic structure and electronic density of states of a material.

2.1 Atomic Structure and Electronic Properties of Single-Walled Carbon Nanotubes

Atomically resolved images of in situ vapor-deposited carbon structures believed to be multi-walled carbon nanotubes (MWNTs) were first reported by Sattler and Ge [16]. Bias-dependent imaging [17] and STS investigations [18] of independently characterized arc generated MWNTs suggested that some fraction of MWNTs produced by the arc method were semiconducting, and in these semiconducting nanotubes, the STS data suggested that the energy gap depended inversely on diameter. Subsequent STM and STS studies of MWNTs and SWNTs have provided indications of different structures and structure-dependent electronic properties, but have not revealed an explicit relationship between structure and electronic properties. The failure of these previous studies to elucidate clearly the expected diameter and helicity dependent electronic properties of nanotubes can be attributed in part to the lack of pure SWNT samples, since (1) the electronic band structure of MWNTs is considerably more complex than SWNTs, and (2) relatively pure samples are required to carry out unambiguous STM and STS measurements.

The development of techniques to produce and purify relatively large quantities of SWNTs has made possible definitive testing of the remarkable predicted electronic properties of nanotubes [19–21]. Indeed, seminal STM and STS measurements of the atomic structure and electronic properties of purified SWNTs by Wildöer et al. [10] and Odom et al. [11] have shown that the electronic properties do indeed depend sensitively on diameter and helicity. In both of these studies, the SWNTs were grown by laser vaporization, ultrasonically suspended in organic solvents, and then deposited by spin coating onto Au (111) substrates. Subsequent STM imaging studies were carried out at low-temperature, in ultra-high vacuum STMs.

2.1.1 Carbon Nanotube Atomic Structure

A large scale STM image of individual tubes and small ropes containing a number of individual SWNTs is shown in Fig. 2a. A high-resolution image of a SWNT (Fig. 2b) exhibits a graphite-like honeycomb lattice, thus enabling the determination of the (n,m) indices from the image. The (n,m) indices were obtained from the experimentally measured values of the chiral angle and diameter. The chiral angle was measured between the zigzag (n,0) direction (the dashed line connecting sites separated by 0.426 nm) and the tube axis.

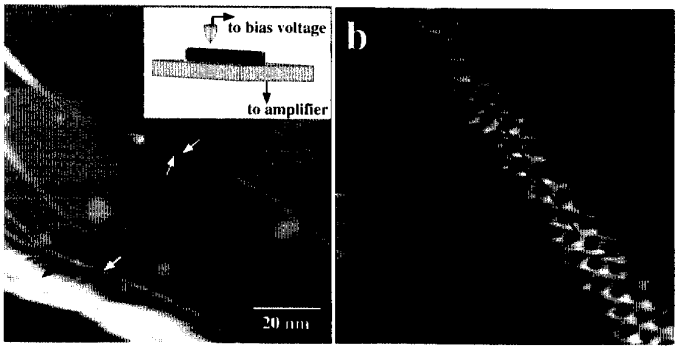

Fig. 2. STM images of nanotubes. (**a**) Large area showing several small bundles and isolated SWNTs on a stepped Au (111) surface. The white arrows indicate individual SWNTs and the black arrows point to small ropes of SWNTs. (inset) Schematic diagram of the STM experiment [13]. (**b**) SWNT on the surface of a rope. The solid, black arrow highlights the tube axis and the dashed line indicates the zigzag direction [11]

The angle measurements were confined to the tops of the atomically resolved nanotubes, which minimizes contributions from the sides of the highly curved tubes, and over distances at least 20 nm to eliminate possible twist-deformation contributions. The SWNT diameters were determined from the projected widths of the nanotube images after deconvoluting the tip contribution to the image. This approach yields a more robust diameter than that determined from the cross-sectional height, since the apparent height is highly dependent upon imaging conditions.

Atomically resolved images of isolated SWNTs on a Au (111) substrate are shown in Figs. 3a and 3b. The measured chiral angle and diameter of the tube in Fig. 3a constrain the (n,m) indices to either (12,3) or (13,3). Note that a (12,3) tube is expected to be metallic, while a (13,3) tube should be semiconducting. On the other hand, the chiral angle and diameter of the SWNT in Fig. 3b constrain the indices to (14,-3). This tube has helicity opposite to the SWNT in Fig. 3a.

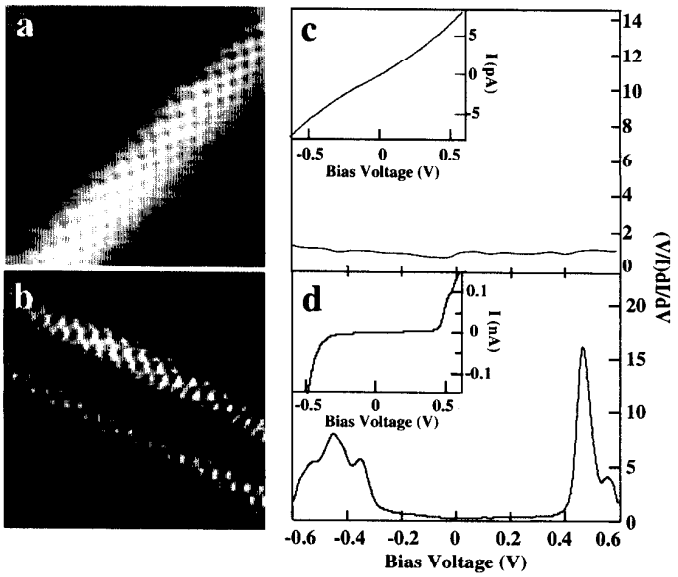

Fig. 3. STM imaging and spectroscopy of individual nanotubes. (**a,b**) Constant current images of isolated nanotubes. The Au (111) lattice is clearly seen in (**a**). (**c,d**) Calculated normalized conductance, (V/I)dI/dV and measured I-V (inset) recorded on the nanotubes in (**a,b**) [11,29]

2.1.2 Spectroscopy: Metals and Semiconductors

Subsequent characterization of the electronic properties of the atomically resolved tubes by tunneling spectroscopy can determine whether the electronic properties depend on structure. Tunneling current versus voltage data recorded along the two tubes discussed above exhibit very different characteristics (Figs. 3c and 3d), and the LDOS that is determined from these I-V data sets are quite distinct. For the tube assigned as (12,3) or (13,3), the LDOS is finite and constant between -0.6 and +0.6 V. This behavior is characteristic of a metal, and thus shows that the (12,3) indices provide the best description for the tube. Moreover, the normalized conductance data determined for the (14,-3) tube exhibit an absence of electronic states at low energies but sharp increases in the LDOS at -0.325 and +0.425 V. These sharp increases are characteristic of the conduction and valence bands of a semiconductor, and thus confirm our expectation that (14,-3) indices correspond to a semiconducting SWNT. These key measurements first verified the unique ability of SWNTs to exhibit fundamentally different electronic properties with only subtle variations in structure [7–9].

In addition, the semiconducting energy gaps (E_g) of SWNTs are predicted to depend inversely on the tube diameter, d, and to be independent of helicity. A summary of the energy gaps obtained by Odom et al. [11] for tubes

with diameters between 0.7 and 1.1 nm is shown in Fig. 4. Significantly, these

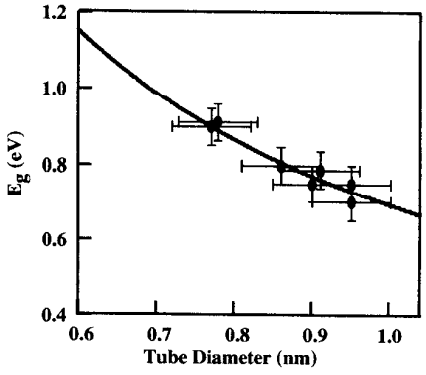

Fig. 4. Summary of energy gap (E_g) versus tube diameter obtained in [11]. The solid line corresponds to a fit described in the text

results and those obtained by Wildöer et al. [10] for tubes with larger diameters between 1 and 2 nm show the expected 1/d dependence. Moreover, these results can be used to obtain a value for the nearest neighbor overlap integral (γ_o) used in tight-binding calculations of the electronic properties by fitting to $E_g=2\gamma_o a_{C-C}/d$, where a_{C-C} is 0.142 nm. The values obtained from the one parameter fit by [11] and [10] respectively, 2.5 eV and 2.7 eV, are in good agreement with the reported values in the literature that range from 2.4-2.9 eV [1,22,23].

2.2 One-Dimensional Band Structure of Nanotubes

The characterization of semiconducting and metallic SWNTs with subtle changes in structure confirms the remarkable electronic behavior of the nanotubes, and represents a significant step forward in understanding these 1D materials. In addition, the ability to probe simultaneously atomic structure and electronic properties provides a unique opportunity to investigate further several interesting properties of these 1D materials. These properties include, for example, the detailed density of states (DOS) of the nanotubes, the role of symmetry breaking distortions on the electronic character of nanotubes, and the electronic properties of defect and end electronic states. Several of these interesting issues are addressed in the following sections and are compared quantitatively with theory.

By making tunneling spectroscopy measurements over an extended energy range, the one-dimensional nature of the energy bands are observed as sharp peaks in the DOS [10,24,25]. When spectroscopic measurements are made on atomically-resolved nanotubes, it is also possible to compare the experimental DOS quantitatively with that resulting from a simple π-only tight-binding calculation. Kim et al. [25] reported the first detailed experimental comparison with theory on a metallic tube with indices (13,7). This

nanotube is the upper isolated tube that rests on the Au surface shown in Fig. 5a. Current vs. voltage measurements exhibited a linear response at V=0 as expected for a metal and showed steps at larger voltages that correspond to a series of sharp peaks in the dI/dV. These peaks correspond to the VHS resulting from the extremal points in the 1D energy bands.

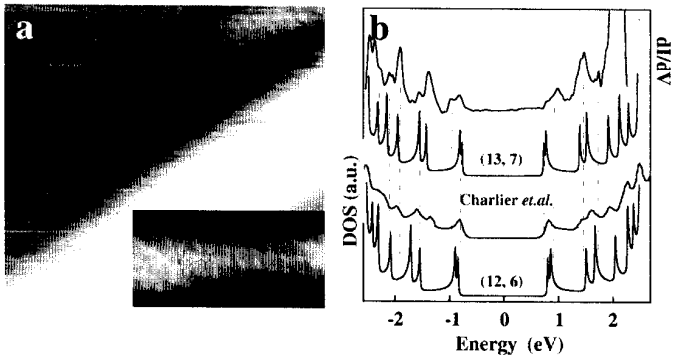

Fig. 5. STM imaging and spectroscopy on a metallic SWNT. (**a**) Tunneling spectra were recorded on the isolated upper tube. The inset shows an atomic resolution image of this tube. A portion of a hexagonal lattice is overlaid to guide the eye. (**b**) Comparison of the DOS obtained from experiment (upper curve) and a π-only tight-binding calculation for the (13,7) SWNT (second curve from top). The broken vertical lines indicate the positions of VHS in the tunneling spectra after consideration of thermal broadening convoluion. The calculated DOS for a (12,6) tube is included for comparison [25]

A direct comparison of these experimental data to the theoretical electronic band structure calculated by a π-only tight-binding model was made [25]. Significantly, the spectroscopy data show good agreement with the calculated DOS for the (13,7) tube (Fig. 5b). The agreement between the VHS positions determined from the calculations and dI/dV data are especially good below E_F, where the first seven peaks correspond well. The peak splitting due to the anisotropy around **K** is also reproduced in the dI/dV. Notably, the experimental gap between the first VHS in this metallic tube, $E_g{}^m \sim$ 1.6 eV, is in agreement with predictions for metallic tubes [26]; that is, $E_g{}^m = 6\gamma_o a_{C-C}/d$ = 1.6 eV, where γ_o =2.5 eV, the value determined from the semiconducting energy gap data [11]. Above the Fermi energy some deviation between the experimental data and calculations exist, but the observed differences may be due to band repulsion, which arises from curvature-induced hybridization [27].

Kim et al. [25] also compared their results to a published $\sigma + \pi$ calculation for a (13,7) SWNT [28] and a π-only calculation for a closely related set of indices. Although detailed comparison is difficult due to the large DOS

broadening, all peaks within ± 2 eV match well with the π-only calculation. This comparison suggests that curvature-induced hybridization is only a small perturbation within the experimental energy scale ($|V| < 2V$) for the (13,7) tube. The sensitivity of the VHS to variations in the (n,m) indices was investigated by calculating the DOS of the next closest metallic SWNT to the experimental diameter and angle; that is, a (12,6) tube. Significantly, the calculated VHS for this (12,6) tube deviate much more from the experimental DOS peaks than in the case of the (13,7) tube. It is worth noting that the poor agreement in this case demonstrates that subtle variations in diameter and helicity do produce experimentally distinguishable changes in the DOS.

Van Hove singularities in the electronic DOS of semiconducting nanotubes have also been observed [10,29]. Odom et al. [29] have characterized spectroscopically a small-diameter (10,0) semiconducting nanotube (Fig. 6a), and directly compared the DOS with a tight-binding calculation. The normalized

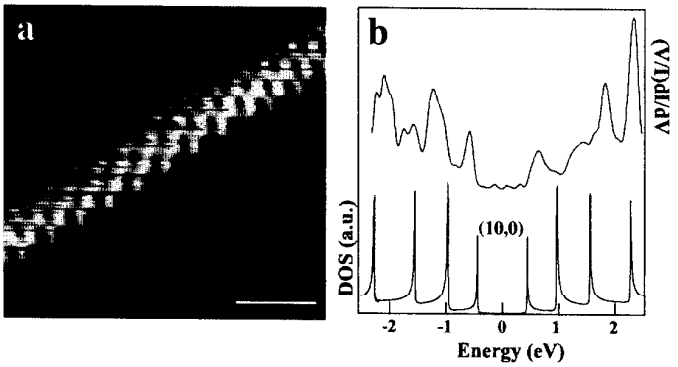

Fig. 6. STM image and spectroscopy of a semiconducting nanotube. (**a**) Image of a SWNT on the surface of a rope. (**b**) Comparison of the DOS obtained from experiment (upper curve) and calculation for the (10,0) SWNT (lower curve) [29]

conductance exhibits relatively good agreement with the calculated (10,0) DOS below E_F but poorer agreement above (Fig. 6b). However, the π-only DOS calculation does not include π/σ and π^*/σ^* mixing due to curvature. This hybridization of π/σ orbitals is believed to produce more pronounced effects on the conduction band [27], and this might explain the observed deviations. Additional work is needed to resolve this point. These results show clearly that the VHS peaks in the electronic band structure, which are characteristic of 1D systems, can be measured experimentally and agree well with the DOS calculated using π-only tight-binding models.

2.3 Localized Structures in Nanotubes

The above results focus on the properties of defect-free, nearly infinite SWNTs. Nanotubes can, however, exhibit a variety of structural defects. For example, the insertion of a pentagon-heptagon (5-7) pair in the hexagonal network [30,31] can produce a kink in the tubular nanotube structure. Also, more gradual bends can result from mechanical distortions and bending. In addition, structural deformations such as bends, twisting, and collapse have been observed occasionally in these seemingly infinite carbon cylinders [32–34]. These defects may develop during growth, processing, deposition, or following an interaction with surface features [35]. The electronic properties of localized SWNT structures, such as bends and ends [36–38], are essential to proposed device applications. Below selected examples of structures that have been characterized with atomically-resolved imaging and spectroscopy are described.

2.3.1 Bent and Twisted Nanotubes

Odom et al. [29] recently reported a kink in an atomically-resolved SWNT rope arising from a mechanical distortion (Fig. 7). The bend angle defined by this kink is approximately 60°. Tunneling spectroscopy was used to characterize the electronic properties of the uppermost nanotube in the bent rope. I-V measurements were performed at the positions indicated by the symbols in Fig. 7a, and their corresponding dI/dV are displayed in Fig. 7b. The positions of the van Hove peaks indicate that the tube is metallic. Significantly, the data also show new features at low bias voltages on either side of the bend. These peaks are likely due to the presence of the bend, since five nanometers away (+) from the kink, the sharpness and prominence of these features have greatly diminished. In addition, Avouris et al. [40] reported that STS spectra taken near a kink in a semiconducting nanotube also showed an increased DOS at low energies. Notably, recent calculations on bends in armchair tubes show similar low energy features in the DOS for similar bend angles [39] observed by [29] and [40].

The bend region observed by Odom and co-workers was further investigated using bias-dependent STM imaging. On the right side of the bend, a superstructure on the tube is observed at the biases of the localized peaks (Figs. 7c and 7d). Fig. 7c shows stripes parallel to the zigzag direction of the tube and Fig. 7d displays a triangular ring structure, where the spacing between nearest-neighbor rings is ca. 0.42 nm (the zigzag spacing). These new electronic features could be due to electron scattering and interference at the defect site [41]. Although the bias voltage, 0.45 V, at which Fig. 7e was imaged is not at a prominent peak in the dI/dV, some electronic structure can be seen extending ~1.5 nm to the right of the bend. However, this additional structure diminishes and an unperturbed atomic lattice is observed, consistent with the spectroscopic measurements. Further experimental and

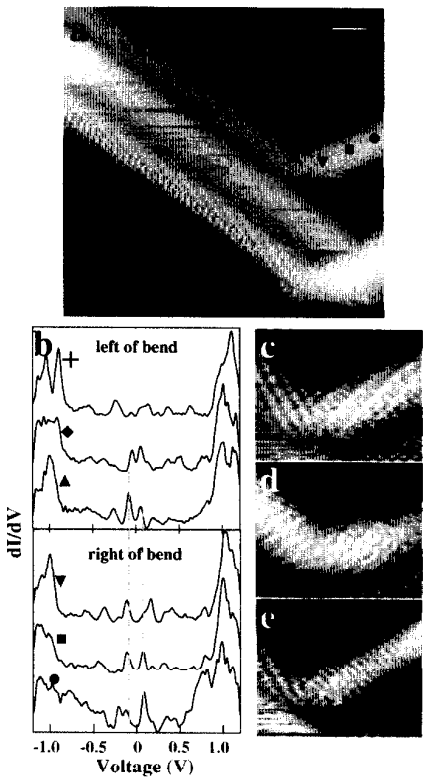

Fig. 7. STM image and spectroscopy of a bend in a rope of SWNTs. (**a**) Image of ~60° bend. The symbols correspond to locations where I-V were measured. The scale bar is 1 nm. (**b**) Differential conductance calculated from the locations indicated in (**a**). The upper portion of the graph is spectroscopy performed on the left side of the bend over 5 nm. The lower portion of the graph is spectroscopy performed on the right side of the bend over 2 nm. The dashed lines highlight the low energy features. (**c-e**) STM images recorded at bias voltages of -0.15, 0.15, and 0.45 V, respectively [29]

computational work is needed to elucidate clearly such interesting observations.

Besides bends in nanotubes, twisting of individual tubes within ropes has been reported by Clauss et al. [33]. Large-scale nanotube twists may result from mechanical interactions during deposition upon surfaces, be introduced during the growth process and frozen by shear forces, or result from different helicity tubes attempting to align their hexagonal lattices within ropes. Clauss et al. [33] observed anomalous lattice orientations upon careful inspection of many tubes, namely, that the armchair direction is on average perpendicular to the tube axis, and that the average angle between the zigzag and armchair direction is greater than 90°. This apparent distortion from an equilibrium conformation can be explained if the imaged nanotubes are of the armchair-type with a twist distortion of several degrees, or from distortions contributed by the finite size and asymmetry of the STM tip.

2.3.2 SWNT Ends: Structure and Electronic Properties

Another example of localized geometric structures in nanotubes is the ends. Analogous to the surface states of a 3D crystal and the edge state of a 2D electron gas, end states are expected at the end of the 1D electron system. The ends of a 1D electronic system can be considered as the "surface" of the 1D bulk. Both resonant and localized states are possible at the ends of nanotubes. Resonant end states are expected for metallic nanotubes because there are no gaps in the 1D band structure of metallic SWNTs to localize the end states. In the same way, localized end states are possible for semiconducting nanotubes since they exhibit energy gaps in their DOS.

The end states associated with carbon nanotubes may arise from pentagons in a capped end or an open nanotube [42,43]. In accordance with Euler's rule, a capped end should contain six pentagons. The presence of these topological defects can cause dramatic changes in the LDOS near the end of the nanotube. Kim et al. [25] reported the first detailed investigation of the electronic character of a capped SWNT end (Fig. 8a), with bulk indices (13,-2). The expected metallic behavior of the (13,-2) tube was confirmed in (V/I)dI/dV data recorded away from the end (Fig. 8c). Significantly, spectroscopic data recorded at and close to the SWNT end show two distinct peaks at 250 and 500 mV that decay and eventually disappear in the bulk DOS recorded far from the tube end.

To investigate the origin of these new spectroscopic features, tight-binding calculations were carried out for a (13,-2) model tube terminated with different end caps (Fig. 8b). Both models exhibit a bulk DOS far from the end (lower curve in Fig. 8d); however, near the nanotube ends the LDOS show pronounced differences from the bulk DOS: Two or more peaks appear above E_F, and these peaks decay upon moving away from the end to the bulk. These models were chosen to illustrate the relatively large peak differences for caps closed with isolated versus adjacent pentagons. The LDOS obtained for cap I shows excellent agreement with the measured LDOS at the tube end, while cap II does not (Fig. 8d). The positions of the two end LDOS peaks as well as the first band edge of cap I match well with those from the experimental spectra. These results suggest that the arrangement of pentagons is responsible for the observed DOS peaks at the SWNT ends, and are thus similar to conclusions drawn from measurements on MWNTs that were not atomically resolved [43].

Besides characterization of capped ends in metallic tubes, Avouris and coworkers [40] reported spectroscopic data on an atomically-resolved semiconducting SWNT and its end. Interestingly, as tunneling spectra were recorded along the tube axis to the end, the Fermi level position shifted to the center of the energy gap. This is the first reported evidence of band-bending behavior observed by STM spectroscopy in individual nanotubes. Future studies could provide important and much needed information addressing the nature of nanotube-metal contacts.

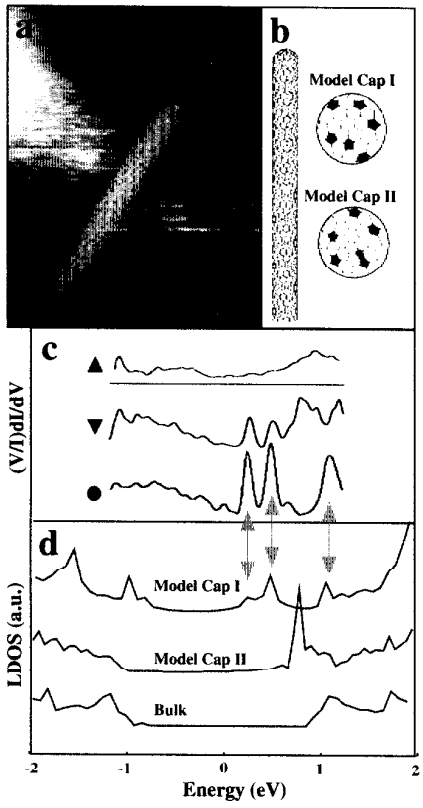

Fig. 8. STM image and spectroscopy of a SWNT end. (**a**) Image of a nanotube end. The symbols correspond to the locations where the tunneling spectra in (**c**) were recorded. The scale bar is 1 nm. (**b**) A model (13,-2) SWNT recorded two different cap configurations; the pentagons are shaded gray. (**c**) Experimental tunneling spectra from the end •, near the end ▼, and far from the end ▲. (**d**) LDOS obtained from tight-binding calculations on capped (13,-2) tubes for caps I and II. Similar features in • and cap I are highlighted by gray arrows. The bulk DOS for both cap models are identical and is shown in the lowest curve [25]

2.4 Finite Size SWNTs

The studies reviewed above have focused on SWNTs that have always retained characteristic features of a periodic 1D system. What happens when this 1D system is made increasingly smaller? Conceptually, as the length of a SWNT is reduced one ultimately will reach the limit of a fullerene molecular cluster–a 0D object. In this regard, studies of finite-size SWNTs offer a unique opportunity to probe the connection between and evolution of electronic structure in periodic molecular systems. Investigations of finite-sized effects in SWNTs are also important to the future utilization of nanotubes in device applications. Low-temperature transport experiments on metallic SWNTs have shown that μm long tubes behave as islands in single electron transistors, with an island energy level spacing characteristic of the 1D particle-in-a-box states [44,45]. Since the coulomb charging energy $E_c \propto 1/L$ (L is the nanotube length), shorter nanotubes allow the working temperature of such devices to increase. In addition, finite size effects should be visible at

room temperature if $\Delta E > k_B T$; thus a resonant tunneling device may be conceived with nanotubes whose lengths are less than 50 nm.

To first order, the 1D energy levels and spacing may be described by either quantization of the metallic band structure or by recollection of the textbook particle in a 1D well. To first order, the bulk metallic nanotube band structure is characterized by two linear bands (π and π^*) that cross the Fermi energy, and these bands contribute a finite, constant DOS at low energies. Confinement of the electrons due to reduced axial lengths produces a discretization $\Delta k = \pi/L$ on the crossing bands. The intersection of Δk and the linear bands in the zone-folding scheme results in an energy level spectrum. An alternative, simpler analysis of this problem is to consider the finite-length nanotube as a 1D particle-in-a-box, whose well-known eigenvalues (E) are $E = \hbar^2 k^2/2m$. The energy level spacing is easily derived:

$$\Delta E = \hbar^2 k_F \Delta k/m = h v_F/2L \approx 1.67 eV/L(nm) \quad (2)$$

where h is Planck's constant and $v_F = 8.1 \times 10^5$ m/s is the Fermi velocity for graphene.

2.4.1 Quantum Effects in Carbon Nanotubes

STM can probe the transition from 1D delocalized states to molecular levels since voltage pulses can first be used to systematically cut nanotubes into short lengths [29,46] (Fig. 9). Subsequently, these finite-size nanotubes can be characterized spectroscopically.

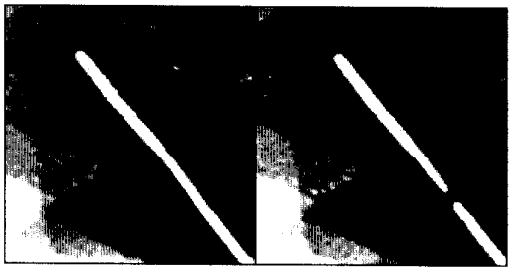

Fig. 9. SWNTs before and after a voltage pulse was applied to cut the nanotube [46]

Venema et al. [47] first reported investigations of quantum size effects in a ~30 nm metallic, armchair nanotube shortened by STM voltage pulses. Current vs. voltage measurements carried out near the middle of the tube showed an irregular step-like behavior. The steps in the spectra observed over a small voltage range (±0.2 V) correspond to quantized energy levels entering the bias window as the voltage is increased, and the irregularity in the step spacing is due to coulomb charging effects competing with the 1D level

spacing. Remarkably, they discovered that compilation of 100 consecutive I-V measurements spaced 23 pm apart into a spectroscopic map exhibited dI/dV peaks which varied periodically with position along the tube axis (Fig. 10a). This periodic variation in dI/dV as a function of position along the tube, 0.4 nm, is different from the lattice constant a_o=0.25 nm (Fig. 10b), and can be

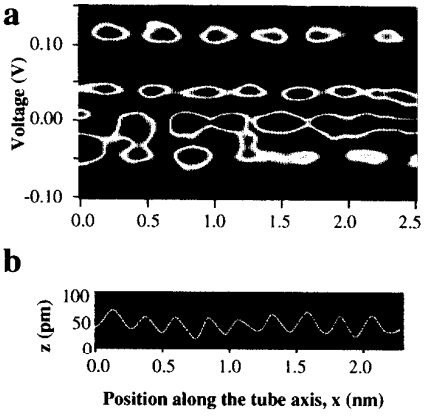

Fig. 10. STM line scans. (**a**) Spectroscopic image compiled from 100 dI/dV measurements. The periodicity is determined from the square of the amplitude of the electron wavefunction at discrete energies. (**b**) Topographic line profile of atomic corrugation in a shortened armchair nanotube [47]

described by the electronic wavefunctions in the nanotube. Since dI/dV is a measure of the squared amplitude of the wavefunction, they were able to fit the experimental dI/dV with the trial function $A\sin^2(2\pi x/\lambda + \phi) + B$. This enabled the separation between the dI/dV peaks to be correlated with half the Fermi wavelength λ_F. The calculated value for $\lambda_F = 3a_o = 0.74$ nm, determined from the two linear bands crossing at k_F, is in good agreement with experimental observations. Hence discrete electron standing waves were observed in short armchair nanotubes. It is also worth noting that the observed widths of the nanotubes probed in these investigations, ~10 nm, are significantly larger than expected for a single SWNT. This suggests that it is likely the measurements were on ropes of SWNTs. In this regard, it will be important in the future to assess how tube-tube interactions perturb the quantum states in a single SWNT.

It is possible that additional features in the electronic structure of finite-sized nanotubes may appear in lengths nearly an order of magnitude shorter. To this end, Odom et al. [29] have studied quantum size effects in both chiral metallic and semiconducting tubes. STM images of nanotubes shortened to six and five nanometers, respectively, are shown in Figs. 11a and 11b. The I-V measurements show a step-wise increase of current over a two-volt bias range for both tubes, and the observed peaks in the (V/I)dI/dV were attributed to resonant tunneling through discrete energy levels resulting from the finite length of the SWNT. To first order, analysis of the peak spacing for the finite-sized nanotubes (Figs. 11d and 11e) agrees with the simple 1D particle-in-

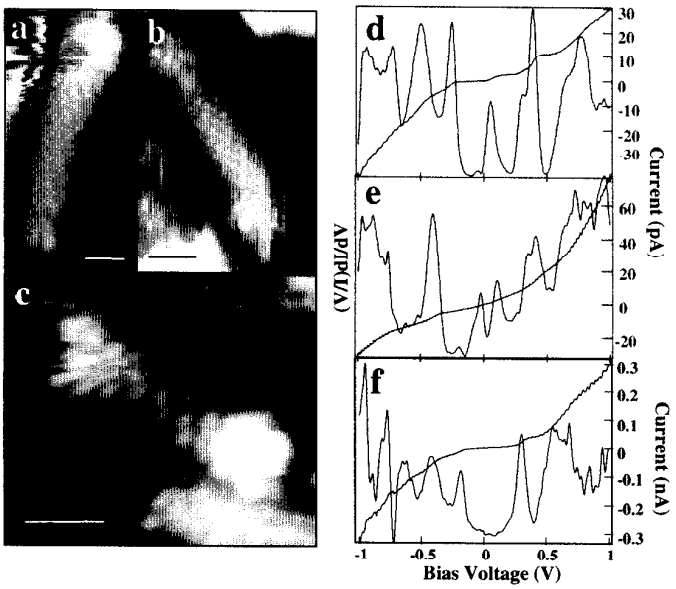

Fig. 11. STM imaging and spectroscopy of finite-size SWNTs. (**a-c**) SWNTs cut by voltage pulses and shortened to lengths of 6 nm, 5 nm, and 3 nm, respectively. (**d-f**) Averaged normzlied conductance and I-V measurements performed on the nanotubes in (**a-c**), respectively. Six I-V curves were taken along the tube length and averaged together since the spectra were essentially indistinguishable [29]

a-box model. The former tube that is six nanometers long exhibits a mean peak spacing of approximately 0.27 eV. A six nanometer tube within this 1D box model would have an average level spacing $\Delta E \sim 1.67$ eV$/6 = 0.28$ eV. For the latter tube with its shorter length, the observed peak spacing is also wider, as expected from this model.

In addition, an atomically resolved SWNT, only three nanometers long was investigated (Fig. 11c). The normalized conductance of this short piece shown in Fig. 11f appears, however, quite different from the expected 1.67 eV$/3 = 0.55$ eV energy level spacing for a nanotube three nanometers long. This is not surprising due to the limitations of this simple model, and the need for a more detailed molecular model to explain adequately the electronic structure is evident. Ab initio calculations of SWNT band structure have recently shown that the energy level spacing of finite-size tubes may be considerably different from that predicted from a Hückel model due to the asymmetry and shifting of the linear bands crossing at E_F [48]. In addition, several molecular computational studies have predicted that nanotubes less than four nanometers long should open a HOMO-LUMO gap around E_F, although its magnitude varies greatly among different calculation methods [49,50]. These studies have been performed on finite-sized, open-ended,

achiral (n,0) zigzag and (n,n) armchair tubes. In quantum chemistry calculations, symmetry considerations are important, and in this regard, chiral nanotubes may exhibit drastically different electronic characteristics compared with achiral ones. Clearly, more sophisticated molecular and first principle calculations are required to fully understand nanotubes at such ultra-short length scales.

In contrast to the metallic nanotubes and other nanoscale systems [51], no significant length dependence is observed in finite-sized semiconducting nanotubes down to five nanometers long [52]. Namely, tunneling spectroscopy data obtained from the center of the shortened tube showed a striking resemblance to the spectrum observed before cutting. That is, the positions of the valence and conduction bands are nearly identical before and after cutting. Spectra taken at the ends also exhibited the same VHS positions, and a localized state near $\sim$0.2 eV, which is attributed to dangling bonds, was also observed. It is possible that long-length scale disorder and very short electron mean free paths ($\sim$2 nm) in semiconducting tubes [53] may account for the similar electronic behavior observed in short and long nanotubes. This suggests that detailed studies should be carried out with even shorter tube lengths. However, recent ab initio calculations on the electronic structure of semiconducting nanotubes with lengths of two-three nanometers also seem robust to reduced-length effects and merely reproduce the major features of the bulk DOS (i.e. the energy gap) [54].

2.4.2 Coulomb Charging in SWNTs

In the experiments discussed above, the finite-sized nanotubes remained in good contact with the underlying substrate after cutting, and the voltage drop was primarily over the vacuum tunnel junction. If the nanotubes are weakly coupled to the surface, a second barrier for electron tunneling is created and these nanotubes may behave as coulomb islands and exhibit coulomb blockade and staircase features in their I-V [55]. The investigation of finite-sized nanotubes in the presence of charging effects is interesting since both effects scale inversely with length and thus can be probed experimentally, in contrast to 3D metal quantum dots [56,57].

Odom et al. [29] recently reported the first detailed investigation of the interplay between these two effects in nanotubes at ultra-short length scales and compared the tunneling spectra with a modified semi-classical theory for single-electron tunneling. The tunneling current vs. voltage of the nanotube in Fig. 12a exhibits suppression of current at zero bias as well as relatively sharp, irregular step-like increases at larger |V| (Fig. 12b), reminiscent of the coulomb blockade and staircase [55]. Similar to [47], the irregularities in the conductance peak spacing and amplitude are attributed to contributions from the discrete level spacing of the finite-sized nanotube [29].

To compare directly the complex tunneling spectra with calculations, Odom and co-workers [29] modified a semi-classical double junction model [56]

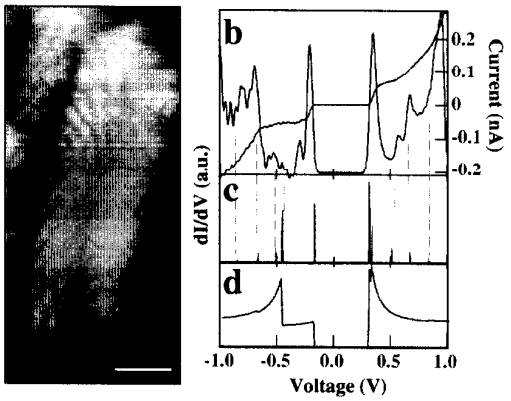

Fig. 12. Charging effects in finite-sized SWNTs. (**a**) STM image of SWNTs shortened by voltage pulses. The scale bar is 1 nm. (**b**) Measured I-V and dI/dV performed on the tube indicated by an arrow in (**a**). (**c**) Numerical derivative of the I-V curve calculated by a semi-classical calculation including the level spacing of a 1D box. (**d**) Same calculation as in (**c**) except the nanotube DOS is treated as continuous [29]

to include the level spacing of the nanotube quantum dot, ΔE $\sim$ 1.67 eV/7 = 0.24 eV. The capacitance of a SWNT resting on a metal surface may be approximated by [58]

$$C = 2\pi\varepsilon L / \ln[d + (d^2 - R^2)^{1/2}]/R \tag{3}$$

where d is the distance from the center of the nanotube to the surface, and ε is 8.85x10^{-3} aF/nm. Estimating d $\sim$ 1.9 nm, the geometric capacitance for the nanotube in Fig. 12a is 0.21 aF. The calculated dI/dV that best fits the tunneling conductance is shown in Fig. 12c, and yields a Au-tube capacitance C_1=0.21 $\pm$ 0.01 aF, in good agreement with the capacitance estimated by the geometry of the nanotube. In contrast, if the calculation neglected the level spacing of the nanotube island, only the blockade region is reproduced well (Fig. 12d). These studies demonstrate that it is possible also to study the interplay of finite size effects and charging effects in SWNT quantum dots of ultra-short lengths.

2.5 Future directions

Scanning tunneling microscopy and spectroscopy have been used to characterize the atomic structure and tunneling density of states of individual SWNTs and SWNT ropes. Defect-free SWNTs exhibit semiconducting and metallic behavior that depends predictably on helicity and diameter. In addition, the 1D VHS in the DOS for both metallic and semiconducting tubes and have compared been characterized and compare reasonably well with tight-binding

calculations. Lastly, studies show that it is possible to access readily a regime of "0D" behavior, where finite length produces quantization along the tube axis, which opens up future opportunities to probe, for example, connections between extended and molecular systems. In short, much of the fascinating overall structural and electronic properties of SWNTs are now in hand–but this really only has scratched the surface. Future work addressing the role of defects and other structural perturbations, coupling to metal and magnetic systems, the connection between extended and finite size/molecular clusters, as well as other directions will help to define further the fundamental physics of these systems and define emerging concepts in nanotechnology.

3 Manipulation of Nanotubes with Scanning Probe Microscopies

Scanning probe microscopies not only can be utilized to probe the fundamental electronic properties of carbon nanotubes but also to manipulate them. The ability to manipulate carbon nanotubes on surfaces with scanning probe techniques enables investigations of nanotube/surface interactions, mechanical properties and deformations, and controllable assembly of nanotube electrical devices. Examples of experiments that have exploited the ability of AFM to connect from the macroscopic world to the nanometer scale and thereby elucidate new behavior and physical properties of nanotubes are discussed below.

3.1 Manipulation of Nanotubes on Surfaces

The interaction between nanotubes and their underlying substrate is sensitive to the details of the particular surface. In order for an AFM tip to controllably manipulate nanotubes across a surface, it is crucial that the tip/nanotube interaction be greater than the adhesion/friction force between the nanotube and the substrate. Depending on the experimental goals, one might, for example, require surfaces with high friction, in order to pin and manipulate the nanotubes into desired configurations. However, if one wants to measure certain physical properties such as stress and strain, a low frictional surface is necessary to decouple the surface contributions from the intrinsic mechanical properties of the nanotube.

Hertel et al. [59] investigated the interaction between a H-passivated Si (100) surface and deposited MWNTs using contact mode AFM. For example, the AFM image of nanotubes in Fig. 13 illustrates one type of elastic deformation that may occur when nanotubes are deposited onto a surface. At the crossing point of the two overlapping MWNTs, the measured height is six nanometers less than the sum of the individual diameters. In addition, the width of the upper nanotube shortly before and after crossing the lower tube appears broadened. This observed axial and radial deformation of the

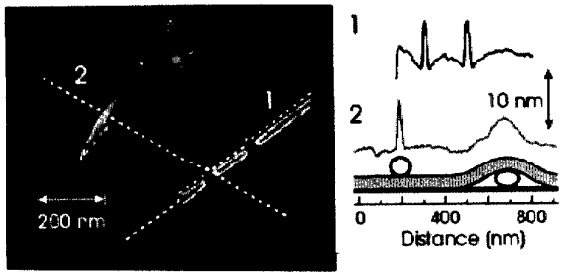

Fig. 13. AFM non-contact mode image of several overlapping MWNTs. The upper tubes are seen to wrap around the lower ones which are slightly compresed [59]

tubes may be explained by a strong surface/nanotube interaction. As the upper nanotube is forced to bend over the lower nanotube, the strain energy increases; however, this is compensated by a gain in binding energy between the surface and the lower nanotube, which attempts to maximize its contact area with the substrate. The strength of the attractive force between the nanotubes and the surface may be estimated using a 1D model where the profile along the tube axis is determined by the balance of strain and adhesion energy. In this framework, Hertel and co-workers [59] found that the binding energy is determined primarily by van der Waals interactions and approaches up to 0.8 ± 0.3 eV/Å for nanotubes 10 nm in diameter on hydrogen-terminated silicon.

An important consequence of this large binding energy is that nanotubes will tend to distort and conform to the substrate topography. In addition, nanotubes can be pinned in highly strained configurations on different substrates after manipulation with an AFM tip [5,59,60]. Wong et al. [5] and Falvo et al. [60] exploited high substrate/nanotube friction in order to apply lateral stresses at specified locations along a MWNT to produce translations and bends (Fig. 14). When bent to large angles, the nanotubes exhibited

Fig. 14. AFM tapping-mode images (0.9 μm x 0.9 μm) of a 4.4 nm-diameter MWNT before and after bending on an oxidized Si substrate. After bending, buckling occurs along the nanotube axis [5]

raised features, which correspond to locations along the nanotube where the tube has buckled. This buckling behavior was shown to be reversible in both experimental studies.

The motion of nanotubes in contact with a surface can occur via rolling, sliding or a combination of these processes. The details of this behavior are expected to depend sensitively on the substrate as well as where the AFM tip contacts the nanotube to induce motion. Falvo et al. [61] found that if the AFM tip pushes the MWNTs from the end on a mica or graphite surface, a single stick-slip peak in the lateral force trace is observed. These peaks are attributed to the pinning force between the nanotube and the substrate that must be overcome before motion can proceed. However, when the nanotube is manipulated from its side on mica, the resulting motion is an in-plane rotation of the nanotube about a pivot point dependent upon the position of the AFM tip. This sliding behavior is illustrated in Fig. 15. However, if the

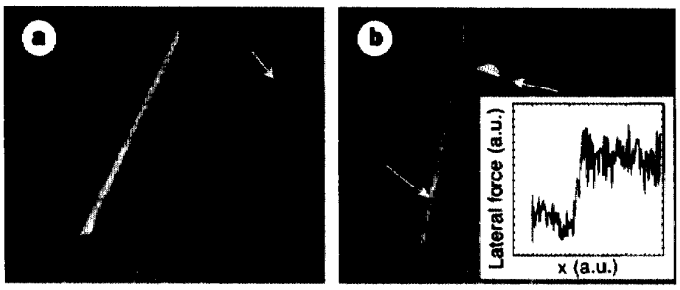

Fig. 15. Sliding a multi-walled carbon nanotube. (**a**) Tube in its original position. Grid lines are overlaid so that one of the grid axes corresponds to the original orientation of the tube axis. (**b**) Tube's orientation after AFM manipulation. The pivot point and push point are indicated by the bottom and top arrows, respectively. Inset shows the lateral force trace during a sliding manipulation [61]

nanotube was pushed from the side on a graphite surface, new behavior was observed: a lateral stick-slip motion with the absence of in-plane rotation. Hence the nanotube appeared to undergo a stick-slip rolling motion, which was topographically verified due to the asymmetrically shaped nanotube cap. Upon comparison of the lateral force measurements for rolling and sliding, Falvo et al. [61] discovered that the slip-stick peaks in rolling are higher than the lateral force needed to sustain sliding, although quantitative force values were not reported. Thus unlike macroscopic systems where rolling is preferred over sliding, the energy cost for rolling in nanoscale systems is larger than that of the sliding cases.

3.2 Nanotube Mechanical Properties

Taking advantage of low substrate/nanotube friction, Wong et al. [5] measured directly the bending and buckling forces for MWNTs on single-crystal MoS_2. They devised a flexible method that uses a combination of conventional lithography to pin one end of the nanotube, and the AFM tip to locate and probe the nanotube region protruding from the static contact. As the AFM scanned normal to the nanotube, the lateral force vs. displacement ($\boldsymbol{F}$-$\boldsymbol{d}$) curves at varying distances from the pinning point was recorded, and information on the Young's modulus, toughness, and strength of the nanotube were obtained. The $\boldsymbol{F}$-$\boldsymbol{d}$ curves recorded on the MWNTs showed several important points (Fig. 16). The initial location at which the lateral $\boldsymbol{F}$ increased

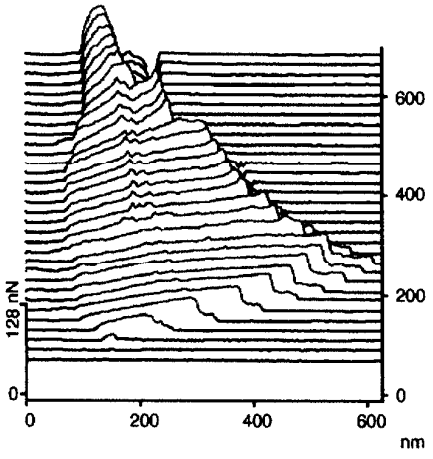

Fig. 16. Surface plot showing the $\boldsymbol{F}$-$\boldsymbol{d}$ response of a 32.9 nm diameter MWNT recorded with a normal load of 16.4 nN. The nanotube is pinned by a SiO pad beyond the top of the image. The data were recorded in water to minimize the nanotube-MoS_2 friction force [5]

in each scan was approximately the same, and thus it was possible to conclude that the nanotube deflection is elastic. Second, the lateral force recorded in each of the individual scans increased linearly once the tip contacted the nanotube ($\boldsymbol{F}$ = k $\boldsymbol{d}$), and k decreased for scan lines recorded at increasingly large distances from the pinning point. From simple nanobeam mechanics formulae, the Young's modulus of MWNTs with diameters from 26 to 76 nm was determined to be 1.28 ± 0.59 TPa, and this value was found to be independent of diameter. The bending strength of nanotubes was also determined by recognizing that the material softens significantly at the buckling point; that is, the buckling point is taken as a measure of the bend strength. The average bending strength, which was determined directly from $\boldsymbol{F}$-$\boldsymbol{d}$ curves, was found to be 14.2 ± 8.0 GPa.

The approach of Wong and co-workers [5] was extended by Walters et al. [62] to assess the tensile strength of SWNT ropes. In these latter measurements, the rope was freely suspended across a trench, and then deflected

with the AFM. Lateral force vs. displacement curves recorded with the AFM tip at several different vertical heights across the center of the tube were modeled reasonably well as an elastic string. The resulting fit to the experimental data yielded a maximum elastic strain of 5.8 ± 0.9 percent. To compare this value with conventional, bulk materials, Walters et al. [62] calculated the yield strength for SWNT ropes, using a Young's modulus of 1.25 TPa for SWNTs [63], and found it to be 45 ± 7 GPa, over 20 times the yield strength of high-strength steels.

3.3 Making Nanotube Devices

The ability to manipulate carbon nanotubes on surfaces is the first step to controllably assemble them into electrical circuits and nanoscale devices. This toolkit has currently been extended to encompass tube translation, rotation, cutting, and even putting nanotubes on top of each other. Recently, Roschier et al. [64] and Avouris et al. [65] exploited nanotube translation and rotation by an AFM probe to create nanoscale circuits where a MWNT served as the active element. Roschier et al. [64] reported the fabrication of a MWNT single electron device (Fig. 17) and characterized its electrical properties. In

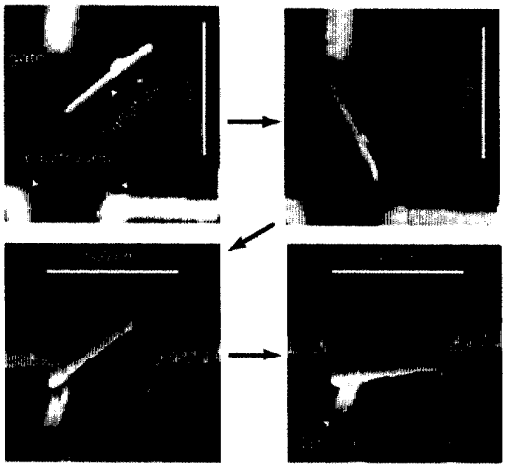

Fig. 17. AFM manipulation of a MWNT over pre-defined electrodes. The 410 nm long MWNT, the side gate, and the electrode struture are marked in the first frame. The last frame represents the measured configuration [64]

addition, Avouris and co-workers [65] have fabricated a variety of structures to investigate the maximum current that can be passed through individual MWNTs, and the possibility of room-temperature electronics. In this latter regard they were able to fabricate a working field-effect transistor from a semiconducting nanotube.

Lefebvre et al. [66] reported the first tapping mode AFM manipulation of SWNT ropes to create crossed nanotube junctions. Their device fabrication strategy was similar to the manipulation method of [64,65], where translation and rotation of nanotubes on surfaces occurred in small increments, typically 10 nm and 5 degrees at a time; however, instead of moving the nanotube over already-deposited electrodes, electrical contact was made to the nanotubes after the manipulation. The top nanotube and degenerate Si substrate can both serve as gate electrodes for the lower nanotube, and the current measured at 5K through the lower nanotube exhibited current peaks reminiscent of two quantum dots in series. The authors speculate that the origin of the junction responsible for the double-dot behavior may either be mechanical (a combination of tube-tube and lower tube-surface interactions) or electrostatic (potential applied between lower tube and upper tube). In any case, the resulting local perturbation changes the nanotube band structure to preclude electron propagation along the lower tube. Interestingly, the tunnel barrier formed by the top bundle on the lower one can be tuned by the substrate voltage, and in the limit of strong coupling, the lower nanotube exhibits charging behavior of a single quantum dot.

As discussed above, manipulation of nanotubes on surfaces allows control in device fabrication of nanotube circuits, although this approach can also damage the nanotubes. Recently, Cheung et al. [67] reported a novel method of AFM manipulation and controlled deposition to create nanotube nanostructures. Their technique eliminates the laborious steps of incremental pushes and rotations as well as the unknown tube damaged caused by AFM manipulation across surfaces. Individual SWNTs and ropes were grown from

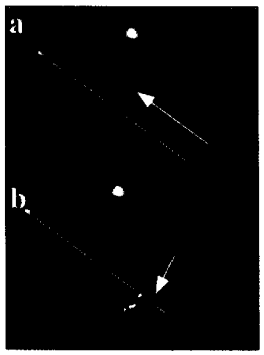

Fig. 18. AFM images of SWNT deposition onto a substrate. (**a**) A SWNT deposited along the direction of the arrow. (**b**) A cross SWNT structure made by a second nanotube lithography step. The images in (**a**) and (**b**) are 2μm x 1.3 μm [67]

Si-AFM tapping mode tips by chemical vapor deposition [68,69]. The SWNTs are deposited from the AFM tip to a pre-defined position on the substrate by three simple steps: (i) biasing the tip against the surface, (ii) scanning the nanotube tip along a set path, and (iii) then applying a voltage pulse to disconnect the tip from the nanotube segment on the substrate. This method

can produce straight structures since tube-surface forces do not need to be overcome, and in addition, complex junctions between nanotubes may be created since the nanotube may be deposited at specified angles (Fig. 18).

4 Nanotube Probe Microscopy Tips

In atomic force microscopy (AFM), the probe is typically a sharp pyramidal tip on a micron-scale cantilever that allows measurement of the tip-sample force interactions and surface topography. Since the resulting image is a convolution of the structure of the sample and tip, sample features are either broadened by the tip, or narrowed in the case of trenches (Fig. 19). A well-

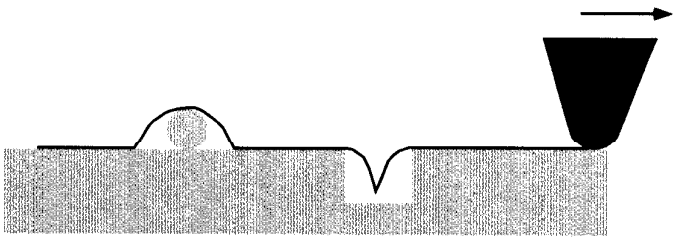

Fig. 19. Tip-sample convolution effect. The black line represents the path of the tip as it scans over the sample. The finite size of the imaging tip will broaden raised features and restrict access to recessed features

characterized tip is therefore essential for accurately interpreting an image, and moreover, the size of the tip will define the resolution of the image. Well-characterized nanostructures, such as a carbon nanotubes, may prove to be the ideal AFM tip.

Integrated AFM cantilever-tip assemblies are fabricated from silicon (Si) or silicon nitride (Si_3N_4) [70]. The tips on these assemblies are pyramidal in shape, have cone angles of 20-30 degrees and radii of curvature of 5-10 nm (Si) or 20-60 nm (Si_3N_4). Several techniques have been developed to improve these geometrical factors such as oxide sharpening, focused ion beam (FIB) milling, electron beam deposition of carbon, as well as improvements in the original tip formation processes. Despite these technological advances, there remain important limitations. Variation in tip-to-tip properties can be quite large, and will always be difficult to control at the scale relevant to high-resolution structural imaging. In addition, tips wear during scanning [71,72], making it quite difficult to account for tip contributions to image broadening. The problems of tip wear increase for sharper tips due to the higher pressure at the tip-sample interface.

Consider the ideal AFM tip. It should have a high aspect ratio with 0^o cone angle, have a radius as small as possible with well-defined and repro-

ducible molecular structure, and be mechanically and chemically robust such that it retains its structure while imaging in air or fluid environments. Carbon nanotubes are the only known material that can satisfy all of these criteria, and thus have the potential to create ideal probes for AFM imaging. For example, nanotubes have exceptional mechanical properties. Recent calculations [73] and experimental measurements [4,5,63] of SWNT and MWNT Young's moduli yield values ranging 1-2 TPa, demonstrating that nanotubes are stiffer than any other known material. The extremely high Young's modulus of nanotubes is critical to the creation of high aspect ratio, sub-nanometer radius tips with high resolution–if the modulus were significantly smaller, the amplitude of thermal vibrations would degrade the resolution of tips. In addition, carbon nanotubes buckle elastically under large loads unlike conventional materials which either fracture or plastically deform. Experimental studies in which nanotubes were used as AFM tips [74] and others which measured the deflection of nanotubes pinned at one end to a surface [5] revealed that the buckling is elastic. Both types of experiments demonstrated that nanotubes can be bent close to 90-degrees many times without observable damage, and thus should be highly robust probes for AFM imaging.

4.1 Mechanical Assembly of Nanotube Tips

In the first demonstration of carbon nanotube AFM tips, Dai et al. [74] manually attached MWNTs to the pyramids of conventional tips. In this process, micromanipulators are used to control the positions of a commercial cantilever-tip assembly and nanotubes while viewing in an optical microscope. Micromanipulators allow the fabrication of nanotube tips that are well aligned for AFM imaging; that is, they are parallel to the tip axis and therefore perpendicular to the sample surface. However, the attached nanotube tips are typically too long to permit high-resolution imaging. The vibration amplitude at the end of the tip, X_{tip}, can be readily estimated by equating $\frac{1}{2}k_BT$ with the potential energy of the fundamental bending mode. This yields

$$X_{tip} = \sqrt{\frac{4k_BTL^3}{3\pi Er^4}} \tag{4}$$

where k_B is Boltzman's constant, T is the temperature in kelvin, L is the length, E is the Young's modulus and r is the radius of the nanotube tip. The length of a nanotube tip can be decreased to reduce the amplitude of vibration to a level where it does not affect resolution by electrical etching on a conductive surface [74,75].

Mechanically assembled MWNT tips have demonstrated several important features. First, the high aspect ratio of the tips enabled more accurate images of structures with steep sidewalls such as silicon trenches [74]. Second, these studies revealed that tip-sample adhesion could be greatly reduced due

to the small size and cylindrical geometry of the nanotube [74,75], which allows imaging at lower cantilever energies. Third, they clearly demonstrated the elastic buckling property of nanotubes, and thus their robustness.

However, MWNT tips were found to provide only a modest improvement in resolution compared with standard silicon tips when imaging isolated amyloid fibrils [76]. The clear route to higher resolution is to use SWNTs, since they typically have 0.5-2 nm radii. Unfortunately, bulk SWNT material consists of bundles approximately 10 nm wide containing up to hundreds of nanotubes each, and thus cannot provide enhanced resolution unless single tubes or small numbers of tubes are exposed at the bundle ends. Wong et al. [77,78] attached these bundles to silicon AFM tips, and adjusted their lengths by the electrical etching procedure described above for optimal imaging. This etching process was found to occasionally produce very high-resolution tips that likely resulted from the exposure of only a small number of SWNTs at the apex . It was not possible in these studies to prepare individual SWNT tips for imaging.

The mechanical assembly production method is conceptually straightforward but also has several limitations. First, it inherently leads to the selection of thick bundles of nanotubes since these are easiest to observe in the optical microscope. Recently, Nishijima et al. [79] mechanically assembled nanotube tips inside a scanning electron microscope (SEM). The use of a SEM still limits assembly to nanotube bundles or individual tubes with diameters greater than 5-10 nm, and moreover, increases greatly the time required to make one tip. Second, well-defined and reproducible tip etching procedures designed to expose individual SWNTs at the tip apex do not exist. Third, a relatively long time is required to attach each nanotube to an existing cantilever. This not only inhibits carrying out the research needed to develop these tips, but also precludes mass production required for general usage.

4.2 CVD Growth of Nanotube Tips

All of the problems associated with mechanical assembly potentially can be solved by direct growth of nanotubes onto AFM tips by catalytic chemical vapor deposition (CVD). In the CVD synthesis of carbon nanotubes, metal catalyst particles are heated in a gas mixture containing hydrocarbon or CO. The gas molecules dissociate on the metal surface and carbon is adsorbed into the catalyst particle. When this carbon precipitates, it nucleates a nanotube of similar diameter to the catalyst particle. Hence, CVD allows control over nanotube size and structure including the production of SWNTs [80], with radii as low as 4 angstroms [81].

The central issues in the growth of nanotube AFM tips by CVD are (1) how to align the nanotubes at the tip such that they are well positioned for imaging and (2) how to ensure there is only one nanotube or nanotube bundle at the tip apex. Two approaches [68,69] for CVD nanotube tip growth have been developed (Fig. 20). First, Hafner et al. [68] grew nanotube tips

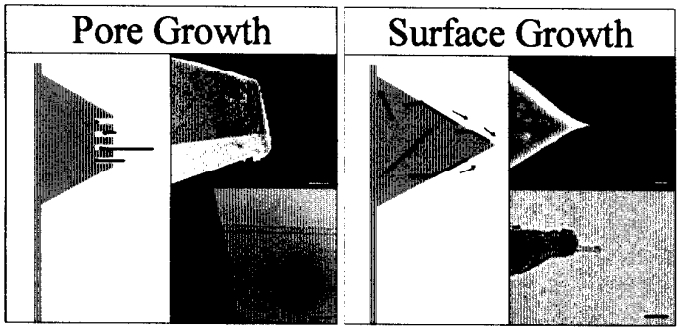

Fig. 20. CVD nanotube tip growth methods. The left panel illustrates pore growth. (top) The SEM image shows a flattened, porous AFM tip with a MWNT protruding from the flattened area. Scale bar is 1 μm. (bottom) The TEM image demonstrates that the tip consists of a thin, single MWNT. Scale bar is 20 nm. The right panel illustrates the surface growth technique. (top) The SEM image demonstrates that nanotubes are steered towards the tip. Scale bar is 100 nm. (bottom) The TEM image reveals that there is an individual SWNT at the tip. Scale bar is 10 nm [68,69]

by CVD from pores created in silicon tips. Electron microscopy revealed that MWNTs grew from pores in the optimal orientation for imaging in these initial studies. These "pore-growth" CVD nanotube tips were shown to exhibit the favorable mechanical and adhesion properties found earlier with manually assembled nanotube tips. In addition, the ability to produce thin, individual nanotube tips has enabled improved resolution imaging [68] of isolated proteins. More recent studies of the pore-growth nanotube tips by Cheung et al. [82] have focused on well-defined iron oxide nanocrystals as catalysts. This effort has enabled the controlled growth of thin SWNT bundles 1-3 nm in diameter from pores made at the silicon tip ends. The pore-growth method has demonstrated the great potential of CVD to produce controlled diameter nanotube tips, although it still has some limitations. In particular, the preparation of a porous layer can be time consuming and may not place individual SWNTs at the optimal location on the flattened apex.

In a second approach, Hafner et al. [69] grew CVD SWNTs directly from the pyramids of silicon cantilever-tip assemblies. The "surface growth" approach has exploited the trade-off between the energy gain of the nanotube-surface interaction and energy cost to bend nanotubes to grow SWNTs from the silicon pyramid apex in the ideal orientation for high resolution imaging. Specifically, when a growing nanotube reaches an edge of a pyramid, it can either bend to align with the edge or protrude from the surface. The pathway followed by the nanotube is determined by a trade-off in the energetic terms introduced above: if the energy required to bend the tube and follow the edge is less than the attractive nanotube-surface energy, then the nanotube will follow the pyramid edge to the apex; that is, nanotubes are steered towards

the tip apex by the pyramid edges. At the apex, the nanotube must protrude along the tip axis since the energetic cost of bending is too high. This steering of nanotubes to the pyramid apex has been demonstrated experimentally [69]. For example, SEM investigations of nanotube tips produced by the surface growth method show that a very high yield of tips contain nanotubes only at the apex, with very few protruding elsewhere from the pyramid. TEM analysis has demonstrated that tips consist of individual SWNTs and small SWNT bundles. In the case of the small SWNT bundles, the TEM images show that the bundles are formed by nanotubes coming together from different edges of the pyramid to join at the apex, thus confirming the surface growth model described above [69]. The surface-growth approach is also important since it provides a conceptual and practical framework for preparing individual SWNT tips by lowering the catalyst density on the surface such that only 1 nanotube reaches the apex [83].

The synthesis of carbon nanotube AFM tips by CVD clearly resolves the major limitations of nanotube tips that arise from the manual assembly method. Rather than requiring tedious mircomanipulation for each tip, it is possible to envision production of an entire wafer of SWNT tips. In addition to ease of production, CVD yields thin, individual SWNT tips that cannot be made by other techniques and represent perhaps the ultimate AFM probe for high-resolution, high aspect ratio imaging.

4.3 Resolution of Nanotube Probes

The high-resolution capabilities of nanotube tips have been evaluated using 5.7 nm diameter gold nanoparticle imaging standards. These are good standards due to their well-defined shape and size, and their incompressibility [84]. The effective tip radius can be calculated from particle images using a two-sphere model [85]. Mechanically assembled MWNT tips typically have shown radii as small as 6 nm, which is expected for the size of arc-produced MWNT material [76]. Manually assembled SWNT tips are composed of thick SWNT bundles made from 1.4 nm nanotubes. The etching procedure can produce high resolution on gold nanoparticles, down to 3.4 nm radius [76,77], although more often the resolution is lower. Pore-growth CVD MWNT have radii ranging 3-6 nm when measured from gold nanoparticle images [68], which is better resolution than manually assembled tips because they are relatively thin and always consist of individual nanotubes. Both the pore-growth [82] and surface growth [69,83] SWNT bundles have shown tip radii of less than 4 nm, reflecting the very thin SWNT bundle or individual SWNT tip structures possible with these methods. These results are summarized in Table 1.

Another significant point regarding nanotube tips is that the range of tip radii measured by AFM has agreed with the range measured by TEM. These results demonstrate that the imaging has been carried out with well-defined probes, which should be amenable to tip deconvolution techniques.

Table 1. Radius of curvature for differently prepared nanotube tips

Nanotube Type	Tip Radius
Mech. Assembled MWNT	> 6 nm
Mech. Assembled SWNT	> 3.5 nm
Pore Growth MWNT	3.5-6 nm
Pore Growth SWNT	2-4 nm
Surface Growth SWNT	2-4 nm
Low Density Surface Growth	< 2 nm

Lastly, the levels of resolution achieved with the nanotubes obtained on gold nanoparticles nearly 6 nm in height, rather than on 1-2 nm features which at times indicate high resolution with tenuous asperities on microfabricated Si and Si_3N_4 tips.

4.4 Applications in Structural Biology

To determine the potential of nanotube tips in structural biology, DNA and several well-characterized proteins have been imaged. DNA was imaged by manually assembled MWNT tips in air [79] and in fluid [86]. The fluid imaging experiments produced a measured height of 2 nm, the expected value based on the intrinsic DNA diameter, and the resolution in these studies was on the order of 3.5 to 5 nm. These values for the resolution are consistent with that expected for multiwalled nanotube material, but are also similar to the best values observed with microfabricated tips [87,72].

Studies of isolated proteins provide a more stringent test of the capabilities of probe tips, and demonstrate clearly the advantages of nanotube tips. Pore-growth MWNT CVD tips have been used to image isolated immunoglobulin-M (IgM) antibody proteins [68]. IgM is a ca. 1 MDa antibody protein with a pentameric structure. It has not been crystallized for X-ray diffraction, but electron microscopy has elucidated the basic features of the pentameric structure [88]. Room temperature studies with pore-growth CVD MWNT nanotube tips [68] have clearly shown the pentameric structure, including five external pairs of antigen binding fragments (Fab domains) and five internal Fc fragments (Fig. 21). In addition, these images occasionally exhibited a structure connecting two of the five Fc domains that could correspond to the joining (J) loop [68]. Because the exact structure of this region is still unclear [88], these investigations have shown the potential of nanotube probes to reveal new structural features on large proteins that cannot be crystallized for diffraction studies.

The resolution of the smaller diameter CVD SWNT tips has been further tested in studies of a smaller protein, GroES, which is a component of the

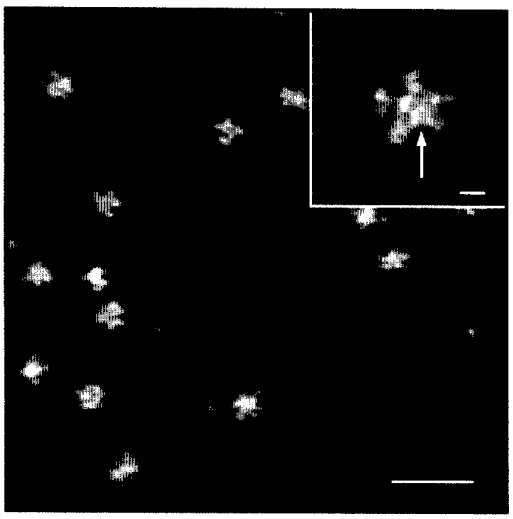

Fig. 21. Images of immunoglobulin-M taken by CVD MWNT tips. Many IgM molecules are seen in various conformations due to their inherent flexibility. Scale bar is 100 nm. The inset shows an example of a well-oriented IgM molecule with the potential J-loop structure highlighted by the white arrow. Scale bar is 10 nm [68]

GroEL/GroES chaperonin system. GroES is a hollow dome shaped heptamer that is approximately 8 nm in outer diameter [89]. The seven 10 kD subunits each consist of a core b-barrel with a b-hairpin loop at the top and bottom. The top b-hairpins point inward to form the top of the dome, while the bottom hairpins are disordered when not in contact with GroEL [90]. CVD SWNT tip images of individual, well-separated GroES molecules on mica [82] reveal that it is possible to resolve the seven-fold symmetry [90] as shown in Fig. 22. These results have demonstrated clearly the ability of the present CVD nanotube tips to achieve sub-molecular resolution on isolated protein systems.

4.5 Applications in Chemical Force Microscopy and Force Spectroscopy

In chemical force microscopy (CFM), the AFM tip is modified with specific chemical functional groups [91]. This enables the tip to generate contrast dependent on the chemical properties of the sample from the friction signal in contact mode or the phase lag signal in tapping mode simultaneously with topography [92]. Functionalized tips have also been employed in force spectroscopy. In this mode of operation the tip is brought into contact with a surface, then retracted. The forces applied to the tip during retraction are due to the interactions of tip and sample molecules. Force spectroscopy has been used to measure a variety of interactions including the intermolecular adhesion between fundamental chemical groups [91,93–95,97], the unfolding of protein molecules [98], antigen-antibody interactions [99], and DNA stretching and unbinding [96].

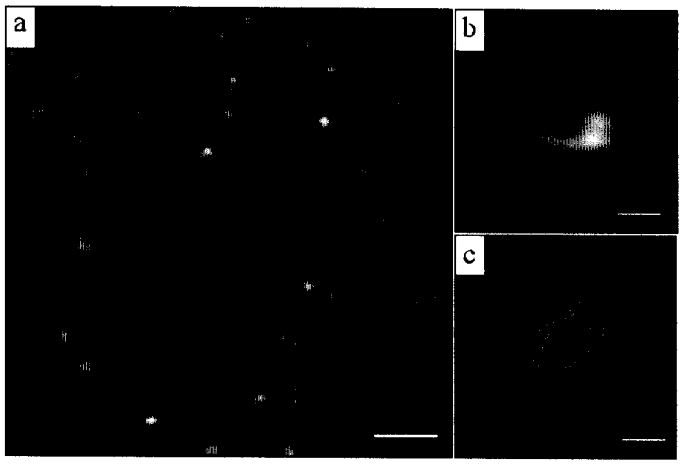

Fig. 22. GroES images taken by CVD SWNT tips. (**a**) A field of many GroES are shown, some displaying the pore side and some displaying the dome. Sclae bar is 50 nm. (**b**) A high resolution image showing the heptameric structure. (**c**) The crystal structure for (**b**) is shown for comparison. [82] Scale bar in (**b**) and (**c**) is 5 nm

Despite the progress made in chemically sensitive imaging and force spectroscopy using silicon and silicon nitride tips, these probes have important limitations. First, the tips have a large radius of curvature making it difficult to control the number of active tip molecules and limiting the lateral resolution. Second, the orientation and often the spatial location of the attached molecules cannot be controlled, leading to uncertainty in the reaction coordinate for force spectroscopy, and increased non-specific interactions. Carbon nanotube tips can overcome these limitations. They have small radii of curvature for higher resolution and can be specifically modified only at their very ends, creating fewer active molecular sites localized in a relatively controlled orientation. Modified SWNT tips could lead to subnanometer resolution in chemical contrast and binding site recognition.

Nanotube tips etched in air are expected to have carboxyl groups at their ends based on bulk studies of oxidized nanotubes [100], although conventional analytical techniques have insufficient sensitivity to observe this for isolated tubes. Chemical species present at the ends of nanotube tips can be studied with great sensitivity by measuring the adhesion of a nanotube tip on chemically well-defined self assembled monolayers (SAMs). Wong et al. [75,78] demonstrated the presence of carboxyl groups at the open ends of manually assembled MWNT and SWNT tips by measuring force titrations as shown in Fig. 23. In the force titration, the adhesion force between a nanotube tip and a SAM surface terminating in hydroxyl groups is recorded as a function of solution pH, thus effectively titrating ionizable groups on the tip [96,97]. Significantly, force titrations recorded between pH 2 and 9 with MWNT and

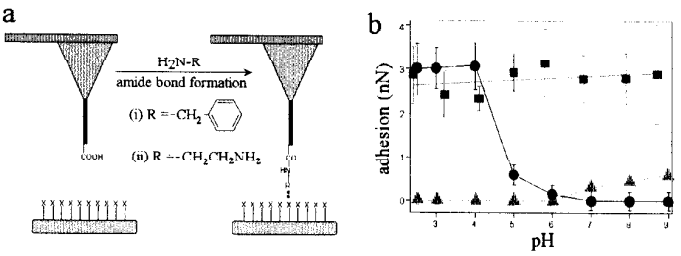

Fig. 23. Chemically-modified nanotube tips. (**a**) Schematic diagram of the bond configuration of -COOH and amine functionalization. (**b**) Force titration data shows the expected adhesion dependence on pH for basic (▲), acidic (•) , and neutral (■) tip functionality [75]

SWNT tips were shown to exhibit well-defined drops in the adhesion force at ca. pH 4.5 that are characteristic of the deprotonation of a carboxylic acid.

Wong et al. [75,78] also modified assembled SWNT and MWNT bundle tips' organic and biological functionality by coupling organic amines to form amide bonds as outlined in Fig. 23a. Nanotube tips modified with benzylamine, which exposes nonionizable, hydrophobic functional groups at the tip end, yielded the expected pH-independent interaction force on hydroxyl-terminated monolayers (Fig. 23). Moreover, force titrations with ethylene diamine-modified tips exhibit no adhesion at low pH and finite adhesion above pH 7 (Fig. 23b), consistent with our expectations for exposed basic amine functionality that is protonated and charged at low pH and neutral at high pH.

Covalent reactions localized at nanotube tip ends represent a powerful strategy for modifying the functionality of the probe. However, the linking atoms that connect the tip and active group introduce conformational flexibility that may reduce the ultimate resolution. In an effort to develop a chemically sensitive probe without conformation flexibility, Wong et al. [101] explored the modification of the tips during the electrical etching process in the presence of O_2, H_2, or N_2. Significantly, force titrations carried out on tips modified in O_2, N_2 and H_2 exhibited behavior consistent with the incorporation of acidic, basic and hydrophobic functionality, respectively, at the tip ends.

Wong et al. [75,78] used functionalized nanotube probes obtain chemically sensitive images of patterned monolayer and bilayer samples [75,78]. Tapping mode images recorded with -COOH and benzyl terminated tips exhibit greater phase lag on the -COOH and $-CH_3$ sample regions, respectively. The "chemical resolution" of functionalized manually assembled MWNT and SWNT tips was tested on partial lipid bilayers [78]. Significantly, these studies showed that an assembled SWNT tip could detect variations chemical functionality with resolution down to 3 nm, which is the same as the best

structural resolution obtained with this type of tip. This resolution should improve with CVD SWNT tips, and recent studies bear this idea out [102].

Lastly, modified nanotube probes have been used to study ligand-receptor binding/unbinding with control of orientation, and to map the position of ligand-receptor binding sites in proteins and on cell surfaces with nanometer or better resolution. To illustrate this point, Wong et al. [75] examined the biotin-streptavidin interaction, which is a model ligand-receptor system that has been widely studied [105]. Biotin-modified nanotube tips were used to probe the receptor binding site on immobilized streptavidin as shown in Fig. 24a [75]. Force spectroscopy measurements show well-defined binding force

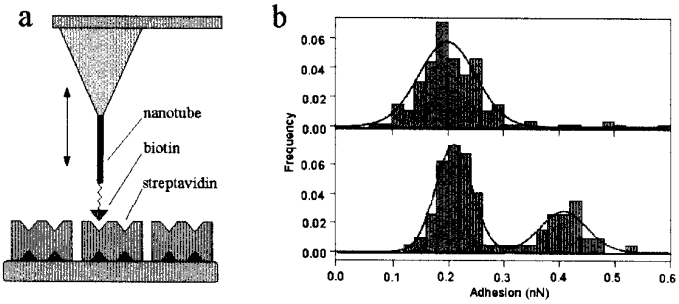

Fig. 24. Nanotube tips in force spectroscopy. (**a**) Nanotube tips are functionalized with biotin and their adhesion is studied against a surface coated with streptavidin. (**b**) The quantized adhesion measurements indicate that single and double biotin-streptavidin binding events are being observed [75]

quanta of ca. 200 pN per biotin-steptavidin pair (Fig. 24b). A key feature of these results compared to previous work [103,104], which relied on nonspecific attachment of biotin to lower resolution tips, is the demonstration that a single active ligand can be localized at the end of a nanotube tip using well-defined covalent chemistry. With the current availability of individual SWNT tip via surface CVD growth, it is now possible to consider the direct mapping of ligand binding sites for a wide range of proteins.

5 Conclusions

Scanning probe microscopies have contributed significantly to understanding a wide range of properties of carbon nanotubes. STM and spectroscopy have been used to characterize the atomic structure and tunneling density of states of individual SWNTs and SWNT ropes. Studies of defect-free SWNTs have demonstrated semiconducting and metallic behavior that depends predictably on helicity and diameter. STM and spectroscopy measurements have defined the 1D VHS in the DOS for both metallic and semiconducting tubes,

and comparisons to tight-binding calculations have shown good agreement with p-only calculations. Deviations from "simple" π-only models also suggest that further work will be necessary to understand fully how tube-tube interactions, which can produce broken symmetry, and curvature effects perturb the electronic structure of SWNTs. STM has also been used to characterize local structure and electronic properties of SWNT bends and ends. These studies have shown the presence of sharp spectroscopic features that in many cases can be understood well using π-only models, although more subtle features, which may reflect electron scattering, will require more detailed experimental and theoretical focus to unravel. The characterization of electronic features at SWNT ends also has implications to understanding and developing the chemical reactivity of this material and to efficiently couple nanotubes for electron transport. In addition, STM has been used to probe the electronic properties of finite length nanotubes. These studies show that it is possible to access readily a regime of "0D" behavior–where finite length produces quantization along the tube axis. These results suggest a number of future opportunities to probe, for example, connections between extended and molecular systems.

AFM has also proven to be a valuable to tool for assessing the mechanical properties of nanotubes and for manipulating nanotubes into new structures. AFM has been used to assess fundamental energetics of nanotube-surface interactions and the frictional properties as nanotubes are slid and/or rolled on surfaces. The high force sensitivity of AFM has also been exploited to assess the Young's modulus of nanotubes and to determine the bending and tensile strengths of MWNTs and SWNTs, respectively. In addition, AFM has been exploited as a tool for positioning nanotube precisely to form nanoscale electronic devices. Lastly, carbon nanotubes have been used as novel probe microscopy tips. CVD methods have been demonstrated to produce well-defined MWNT and SWNT tips in an orientation optimal for imaging. AFM studies using these nanotube tips have demonstrated their robustness and high resolution. This new generation of probes has demonstrated ultrahigh resolution and chemically sensitive imaging capabilities, and is expected to have a significant impact on nanoscale research in Biology, Chemistry and Physics. As one looks to the future, we believe that probe microscopy studies of and with nanotubes will be rewarded with answers to many fundamental scientific problems, and moreover, will push many emerging concepts in nanotechnologies.

References

1. M.S. Dresselhaus, G. Dresselhaus: *Science of Fullerenes and Carbon Nanotubes* (Academic, San Diego 1996)
2. B.I. Yakobson, R.E. Smalley: Amer. Sci. **85**, 324 (1997)
3. C. Dekker: Phys. Today **52**, 22 (1999)
4. M.M.J. Treacy, T.W. Ebbesen, J.M. Gibson: Nature **381**, 678 (1996)

5. E.W. Wong, P.E. Sheehan, C.M. Lieber: Science **277**, 1971 (1997)
6. B.I. Yakobson, C.J. Brabec, J. Bernholc: Phys. Rev. Lett.**76**, 2511 (1996)
7. N. Hamada, S. Sawada, A. Oshiyama: Phys. Rev. Lett. **68**, 1579 (1992)
8. J.W. Mintmire, B.I. Dunlap, C.T. White, Phys. Rev. Lett.**68**, 631 (1992)
9. R. Saito, M. Fujita, G. Dresselhaus, M.S. Dresselhaus: Appl. Phys. Lett. **60**, 2204 (1992)
10. J.W.G. Wildöer, L.C. Venema, A.G. Rinzler, R.E. Smalley, C. Dekker: Nature **391**, 59 (1998)
11. T.W. Odom, J.-L. Huang, P. Kim, C.M. Lieber: Nature **391**, 62 (1998)
12. C.M. Lieber: Solid State Comm. **107**, 607 (1998)
13. J.T. Hu, T.W. Odom, C.M. Lieber: Accts. Chem. Res. **32**, 435 (1999)
14. C.L. Kane, E.J. Mele: Phys. Rev. Lett. **78**, 1932 (1997)
15. V.H. Crespi, M.L. Cohen, A. Rubio: Phys. Rev. Lett. **79**, 2093 (1997)
16. M. Ge, K. Sattler: Science **260**, 515 (1993)
17. Z. Zhang, C.M. Lieber: Appl. Phys. Lett. **62**, 2972 (1993)
18. C.H. Olk, J.P. Heremans: J. Mater. Res. **9**, 259 (1994)
19. A. Thess, R. Lee, P. Nikolaev, H. Dai, P. Petit, J. Rober, C. Zu, Y.H. Lee, S.G. Kim, A.G. Rinzler, D.T. Colbert, G.E. Scuseria, D. Tomanek, J.E. Fischer, R.E. Smalley: Science **273**, 483 (1996)
20. C. Journet, W.K. Maser, P. Bernier, A. Loiseau, M. Lamy de la Chapelle, S. Lefrant, P. Deniard, R. Lee and J.E. Fischer: Nature **388**, 756 (1997)
21. T. Guo, P. Nikolaev, A. Thess, D.T. Colbert, R.E. Smalley: Chem. Phys. Lett. **243**, 49 (1995)
22. C.T. White, J.W. Mintmire: Nature **394**, 29 (1998)
23. C.T. White, D.H. Robertson, J.W. Mintmire, Phys. Rev. B **47**, 5485 (1993)
24. T.W. Odom, J.-L. Huang, P. Kim, M. Ouyang, C.M. Lieber: J. Mater. Res. **13**, 2380 (1998)
25. P. Kim, T.W. Odom, J.-L. Huang, C.M. Lieber: Phys. Rev. Lett. **82**, 1225 (1999)
26. A. Rubio: Appl. Phys. A. Mater. **68**, 275 (1999)
27. X. Blasé, L.X. Benedict, E.L. Shirley, S.G. Louie: Phys. Rev. Lett. **72**, 1878 (1994)
28. J.C. Charlier, Ph.Lambin: Phys. Rev. B **57**, R15037 (1998)
29. T.W. Odom, J.-L. Huang, P. Kim, C.M. Lieber: J. Phys. Chem. B **104**, 2794 (2000)
30. V. Meunier, L. Henrard, Ph. Lambin: Phys. Rev. B **57**, 2596 (1998)
31. J.-C. Charlier, T.W. Ebbeson, Ph. Lambin: Phys. Rev. B **53**, 11108 (1996)
32. T. Hertel, R.E. Walkup, Ph. Avouris: Phys. Rev. B **58**, 13870 (1998)
33. W. Clauss, D.J. Bergeron, A.T. Johnson: Phys. Rev. B **58**, 4266 (1998)
34. N.G. Chopra, L.X. Benedict, V.H. Crespi, M.L. Cohen, S.G. Louie, A. Zettl: Nature **377**, 135 (1995)
35. P. Lambin, V. Meunier, L.P. Biro: Carbon **36**, 701 (1998)
36. P.H. Lambin, A.A. Lucas, J.C. Charlier: J. Phys. Chem. Solids **58**, 1833 (1997)
37. L. Chico, V.H. Crespi, L.X. Benedict, S.G. Louie, M.L. Cohen: Phys. Rev. Lett. **76**, 971 (1996)
38. J. Han, M.P. Anantram, R.L. Jaffe, J. Kong, H. Dai: Phys. Rev. B **57**, 14983 (1998)
39. A. Rochefort, D.R. Salahub, Ph. Avouris: Chem. Phys. Lett. **297**, 45 (1998)
40. Ph. Avouris: Nanotube proceedings

41. C.L. Kane, E.J. Mele: Phys. Rev. B **59**, R12759 (1999)
42. R. Tamura, M. Tsukada: Phys. Rev. B **52**, 6015 (1995)
43. D.L. Carroll, P. Redlich, P.M. Ajayan, J.C. Charlier, X. Blas, A. DeVita, R. Car: Phys. Rev. Lett. **78**, 2811 (1997)
44. M. Bockrath, D.H. Cobden, P.L. McEuen, N.G. Chopra, A. Zettl, A. Thess, R.E. Smalley: Science **275**, 1922 (1997)
45. S.J. Tans, M.H. Devoret, H. Dai, A. Thess, R.E. Smalley, L.J. Geerligs, C. Dekker: Nature **386**, 474 (1997)
46. L.C. Venema, J.W.G. Wildoer, H.L.J. Temminck Tunistra, C. Dekker, A. Rinzler, R.E. Smalley: Appl. Phys. Lett. **71**, 2629 (1997)
47. L.C. Venema, J.W.G. Wildoer, J.W. Janssen, S.J. Tans, H.L.J. Temminck Tuinstra, L.P. Kouwenhoven, C. Dekker: Science **283**, 52 (1999)
48. A. Rubio, D. Sanchez-Portal, E. Attach, P. Ordoejon, J.M. Soler: Phys. Rev. Lett. **82**, 3520 (1999)
49. L.G. Bulusheva, A.V. Okotrub, D.A. Romanov, D. Tomanek: J. Phys. Chem. A **102**, 975 (1998)
50. A. Rochefort, D.R. Salahub, Ph. Avouris: J. Phys. Chem. B **103**, 641 (1999)
51. S.A. Empedocles, D.J. Norris, M.G. Bawendi: Phys. Rev. Lett. **77**, 3873 (1996)
52. T.W. Odom, J.-L. Huang, C.M. Lieber: unpublished
53. P.L. McEuen, M. Bockrath, D.H. Cobden, Y.-G. Yoon, S.G. Louie: Phys. Rev. Lett. **83**, 5098 (1999)
54. R.A. Jishi, J. Bragin, L. Lou: Phys. Rev. B **59**, 9862 (1999)
55. H. Grabert, M.H. Devort: *Single Charge Tunneling* (Plenum, New York, 1992)
56. A.E. Hanna, M. Tinkham: Phys. Rev. B **44**, 5919 (1991)
57. D.C. Ralph, C.T. Black, M. Tinkham: Phys. Rev. Lett. **74**, 3241 (1995)
58. M.H. Nayfeh, M.K. Brussel: *Electricity and Magnetism* (John Wiley and Sons, New York, 1985)
59. T. Hertel, R. Martel, Ph. Avouris: J. Phys. Chem. **102**, 910 (1998)
60. M.R. Falvo, G.J. Clary, R.M. Taylor II, V. Chi, F.P. Brooks Jr, S. Washburn, R. Superfine: Nature **389**, 582 (1997)
61. M.R. Falvo, R.M. Taylor, A. Helser, V. Chi, F.P. Brooks, S. Washburn, R. Superfine: Nature **397**, 236 (1999)
62. D.A. Walters, L.M. Ericson, M.J. Casavant, J. Liu, D.T. Colbert, K.A. Smith, R.E. Smalley: Appl. Phys. Lett. **74**, 3803 (1999)
63. A. Krishnan, E. Dujardin, T.W. Ebbesen, P.N. Yianilos, M.M. J. Treacy: Phys. Rev. B **58**, 14013 (1998)
64. L. Roschier, J. Penttilä, M. Martin, P. Hakonene, M. Paalanen, U. Tapper, E.I. Kauppinen, C.Journet, P. Bernier: Appl. Phys. Lett. **75**, 728 (1999)
65. Ph. Avouris, T. Hertel, R. Martel, T. Schmidt, H.R. Shea, R.E. Walkup: Appl. Surf. Sci. **141**, 201 (1999)
66. J. Lefebvre, J.F. Lynch, M. Llanguno, M. Radosavljevic, A.T. Johnson: Appl. Phys. Lett. **75**, 3014 (1999)
67. C.L. Cheung, J. H. Hafner, T.W. Odom, K. Kim, C.M. Lieber: Appl. Phys. Lett. **76**, xx (2000)
68. J.H. Hafner, C.-L. Cheung, C.M. Lieber: Nature **398**, 761 (1999)
69. J.H. Hafner, C.-L. Cheung, C.M. Lieber: J. Am. Chem. Soc **121**, 9750 (1999)
70. T.R. Albrecht, S. Akamine, T.E. Carber, C.F. Quate: J. Vac. Sci. Tech. A 8, 3386 (1989)
71. H.G. Hansma, D.E. Laney, M. Bezanilla, R.L. Sinsheimer, P.K. Hansma: Biophys. J. **68**, 1672 (1995)

72. Y.L. Lyubchenko, L.S. Schlyakhtenko: Proc. Natl. Acad. Sci. USA **94**, 496 (1997)
73. J.P. Lu: Phys. Rev. Let. **79**, 1297 (1997)
74. H. Dai, J.H. Hafner, A.G. Rinzler, D.T. Colbert, R.E. Smalley: Nature **384**, 147 (1996)
75. S.S. Wong, E. Joselevich, A.T. Woolley, C.-L. Cheung, C.M. Lieber: Nature **394**, 52 (1998)
76. S.S. Wong, J.D. Harper, P.T. Lansbury, C.M. Lieber: J. Am. Chem. Soc. **120**, 603 (1998)
77. S.S. Wong, A.T. Woolley, T.W. Odom, J.-L. Huang, P. Kim, D.V. Vezenov, C.M. Lieber: Appl. Phys. Lett. **73**, 3465 (1998)
78. S.S. Wong, A.T. Woolley, E. Joselevich, C.M. Lieber: J. Am. Chem. Soc **120**, 8557 (1998)
79. H. Nishijima, S. Kamo, S. Akita, Y. Nakayama: Appl. Phys. Lett. **74**, 4061 (1999)
80. J.H. Hafner, M.J. Bronikowski, B.R. Azamian, P. Nikolaev, A.G. Rinzler, D.T. Colbert, K. Smith, R.E. Smalley: Chem. Phys. Lett. **296**, 195 (1998)
81. P. Nikolaev, M.J. Bronikowski, R.K. Bradley, F. Rohmund, D.T. Colbert, K.A. Smith, R.E. Smalley: Chem. Phys. Lett. **313**, 91 (1999)
82. C.-L. Cheung, J.H. Hafner, C.M. Lieber: Proc. Natl. Acad. Sci., **97**, 3809 (2000)
83. J.H. Hafner, C.-L. Cheung, C.M. Lieber: in preparation (2000)
84. J. Vesenka, S. Manne, R. Giberson, T. Marsh, E. Henderson: Biophys. J. **65**, 992 (1993)
85. C. Bustamante, D. Keller, G. Yang: Curr. Opin. Stuct. Biol. **3**, 363 (1993)
86. J. Li, A.M. Cassell, H. Dai: Surf. InterFac. Anal. **28**, 8 (1999)
87. W. Han, S.M. Lindsay, M. Klakic, R.E. Harrington: Nature **386**, 563 (1997)
88. S.J. Perkins, A.S. Nealis, B.J. Sutton, A. Feinstein: J. Mol. Biol. **221**, 1345 (1991)
89. P.B. Sigler, Z. Xu, H.S. Rye, S.G. Burston, W.A. Fenton, A.L. Horwich: Annu. Rev. Biochem. **67**, 581 (1998)
90. J.F. Hunt, A.J. Weaver, S.J. Landry, L. Gierasch, J. Deisenhofer: Nature **379**, 37 (1996)
91. C.D. Frisbie, L.F. Rozsnyai, A. Noy, M.S. Wrighton, C.M. Lieber: Science **265**, 2071 (1994)
92. A. Noy, C.H. Sanders, D.V. Vezenov, S.S. Wong, C.M. Lieber: Langmuir **14**, 1508 (1998)
93. J.B.D. Green, M.T. McDermott, M.D. Porter, L.M. Siperko: J. Phys. Chem. **99**, 10960 (1995)
94. A. Noy, C.D. Frisbie, L.F. Rozsnyai, M.S. Wrighton, C.M. Lieber: J. Am. Chem. Soc. **117**, 7943 (1995)
95. A. Noy, D.V. Vezenoz, C.M. Lieber: Annu. Rev. Mater. Sci. **27**, 381 (1997)
96. A. Noy, D.V. Vezenov, J.F. Kayyem, T.J. Meade, C.M. Lieber: Chemistry *A* Biology **4**, 519 (1997)
97. D.V. Vezenov, A. Noy, L.F. Rozsnyai, C.M. Lieber: J. Am. Chem. Soc. **119**, 2006 (1997)
98. M. Rief, M. Gautel, F. Oesterhelt, J.M. Fernandez, H.E. Gaub: Science **276**, 1109 (1997)
99. P. Hinterdorfer, W. Baumgertner, H.J. Gruber, K. Schilcher, H. Schindler: Proc. Natl., Acad. Sci. USA **93**, 3477 (1996)

100. H. Hiura, T.W. Ebbesen, K. Tanigaki: Adv. Mater. **7**, 275 (1995)
101. S.S. Wong, A.T. Woolley, E. Joselevich, C.M. Lieber: Chem. Phys. Lett. **306**, 219 (1999)
102. C.-L. Cheung, L. Chen, C.M. Lieber: unpublished results (2000)
103. E.-L. Florin, V.T. Moy, H.E. Gaub: Science **264**, 415 (1994)
104. G.U. Lee, D.A. Kidwell, R.J. Colton: Langmuir **10**, 354 (1994)
105. O. Livnah, E.A. Bayer, M. Wilchek, J.L. Sussman: Proc. Natl. Acad. Sci. USA **90**, 5076 (1993)